Assessment of Geometry and In-Flow Effects on Contra-Rotating Open Rotor Broadband Noise Predictions

Nikolas S. Zawodny,[*] Douglas M. Nark,[†] and D. Douglas Boyd Jr.[‡]

NASA Langley Research Center, Hampton, VA, 23681

Application of previously formulated semi-analytical models for the prediction of broadband noise due to turbulent rotor wake interactions and rotor blade trailing edges is performed on the historical baseline F31/A31 contra-rotating open rotor configuration. Simplified two-dimensional blade element analysis is performed on cambered NACA 4-digit airfoil profiles, which are meant to serve as substitutes for the actual rotor blade sectional geometries. Rotor in-flow effects such as induced axial and tangential velocities are incorporated into the noise prediction models based on supporting computational fluid dynamics (CFD) results and simplified in-flow velocity models. Emphasis is placed on the development of simplified rotor in-flow models for the purpose of performing accurate noise predictions independent of CFD information. The broadband predictions are found to compare favorably with experimental acoustic results.

Nomenclature

b_W	wake half-width, m
B_i	number of blades in ith rotor
$c_{i,j}$	chord length of (i,j)th rotor blade section, m
C_d	blade section drag coefficient
J_l	Bessel function of the first kind (order l)
$k_0 = \omega/c_0$	acoustic wavenumber, 1/m
l	azimuthal acoustic interaction mode order
l_r	spanwise correlation length scale, m
L	integral turbulence length scale, m
$\mathcal{L}^{\mathrm{LE}}$	unsteady loading term due to leading edge interaction
$\mathcal{L}^{\mathrm{TE}}$	unsteady loading term due to trailing edge interaction
m	scattering index for front rotor
M_x	axial flight Mach number
r_j	radial location of jth blade section, m
R_i	tip radius of ith rotor, m
S_{pp}	power spectral density of far-field radiated pressure, Pa^{2}s/rad
S_{qq}	wavenumber surface pressure cross-spectrum, N^{2}s/rad
$U_{Xi,j}$	relative in-flow velocity of (i,j)th rotor blade section, m/s
$\overline{w^2}$	mean square velocity of wake turbulence, m^2/s^2
X_η	helical convection distance between rotor blades, m
$\alpha_{i,j}$	pitch angle of (i,j)th rotor blade section relative to axial direction, rad
δ^*	boundary layer displacement thickness, m
$\Theta = u_\theta/\Omega r$	tangential velocity (swirl) coefficient
$\lambda = u_x/\Omega R$	axial velocity in-flow ratio

[*]Research Scientist, Aeroacoustics Branch, Member AIAA; nikolas.s.zawodny@nasa.gov
[†]Research Scientist, Structural Acoustics Branch, Associate Fellow AIAA; d.m.nark@nasa.gov
[‡]Senior Research Engineer, Aeroacoustics Branch, Senior Member AIAA; d.d.boyd@nasa.gov

American Institute of Aeronautics and Astronautics

| Φ_{ww} | wavenumber spectrum of turbulent upwash velocity, $\mathrm{m^4/s^2}$ |
ω	angular frequency, rad/s
Ω_i	angular speed of ith rotor, rad/s
(r_e, θ_e)	emission radius and polar angle, (m, deg)
(r_o, θ_o)	observer radius and polar angle, (m, deg)
$\mathbf{X}_i = (r, X_i, Y_i)$	cylindrical coordinate bound to blade element in radial, chordwise, and normal directions
$\mathbf{x}_i = (r, x_i, \phi_i)$	cylindrical coordinate bound to blade element in radial, axial, and azimuthal directions
$(.)_i$	quantity associated with rotor number ($i = 1$ and 2 for front and rear, respectively)
$(.)_j$	quantity associated with spanwise blade section number

I.   Introduction

CONTRA-ROTATING open rotors (CRORs) have received renewed interest in recent years as a possible alternative to turbofan engines as a means of commercial aircraft propulsion. Compared to turbofan engines with equivalent core technology, open rotor engines are evidenced to provide significant reductions in both fuel consumption and landing-takeoff cycle nitrogen oxide ($\mathrm{NO_X}$) emissions for short-range, single-aisle commercial aircraft.[1] Despite this expected benefit, open rotors have been consistently identified as exhibiting higher noise levels than turbofan engines from both interior cabin and external community noise radiation perspectives. This warrants a need for CROR noise prediction methods that can be used to identify quieter configurations.

To date, noise prediction studies of CRORs have primarily focused on the tonal components of noise.[2,3,4] The source mechanisms of these tonal components have been identified as the steady loading and thickness noise of the rotors (blade passage frequencies and associated harmonics), as well as the unsteady loading noise resulting from interaction of the aft rotor blades with the wakes and vortices shed from the front rotor blades along with the influence of the aft blade row potential field on the front blade row (interaction tones). Until recently,[5] the broadband noise contribution of CRORs has received very little attention because it has been traditionally regarded as negligible compared to tonal noise. However, observation of sample spectral results in Fig. 1 shows that the broadband component of noise becomes the primary contributor for full-scale frequencies at and above 2 kHz. The results shown are from the scaled CROR model studied in Ref. 6 using the scaling regime presented in Ref. 7. The data is from a microphone located in-line with the aft rotor pitch change axis at a distance of 1.524 m from the rotor hub centerline. This spectrum is representative of a CROR in a take-off configuration.
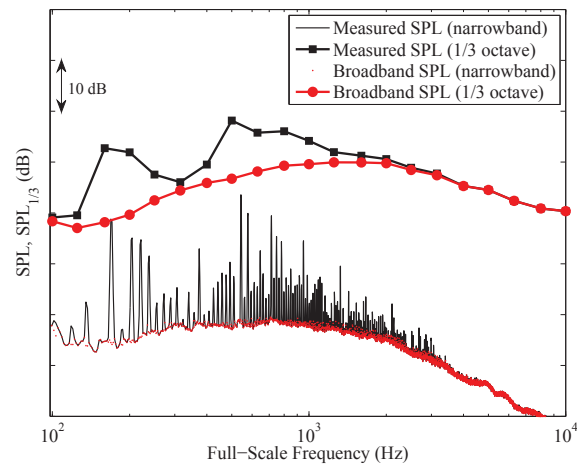
| (a) | (b) |

Figure 1. Illustration of broadband contribution to total noise measured from a scaled CROR model equipped with F31/A31 historical baseline blade set: (a) image of experimental CROR wind tunnel setup, (b) acoustic spectrum taken in-line with aft rotor pitch change axis for the case of $\Omega_1 = \Omega_2 = 6436$ RPM. More details of this testing condition provided in Table 1.

American Institute of Aeronautics and Astronautics

In this paper, the semi-analytical formulations of broadband noise prediction for an isolated CROR configuration introduced by Blandeau et al.[8] are first briefly overviewed. Then, adjustments to these methods are proposed to account for the rotor blade geometries, in-flow conditions and turbulent wake behavior. These attributes will be seen to play an important role in the predictions. The rotor aerodynamic inputs stem from computational fluid dynamic (CFD) supporting data, as well as general rotorcraft momentum theory.[9] It is the goal of this paper to provide a general methodology for obtaining the aerodynamic information required by the prediction methods that can be applied to other CROR configurations. This will allow for the prediction of CROR broadband noise in a computationally efficient manner that is not dependent on CFD results. Finally, the performance of the resulting predictions are gauged through comparison with experimentally measured acoustic spectra.

II.   Broadband Formulations Overview

The works of Blandeau[10] and Blandeau et al.[8] postulate that the two primary sources of CROR broadband noise are: (1) broadband rotor wake interaction noise (BRWI), and (2) broadband rotor trailing edge noise (BRTE). The former of these sources accounts for the noise resulting from impingement of the turbulent wakes shed from the front rotor blades on the leading edges of the aft rotor blades, while the latter accounts for the noise resulting from the interaction of boundary layer turbulence on each rotor blade with its trailing edge. A schematic illustrating the source mechanisms and pertinent geometric and flow parameters for a $B_1 \times B_2$ bladed CROR is provided in Fig. 2.
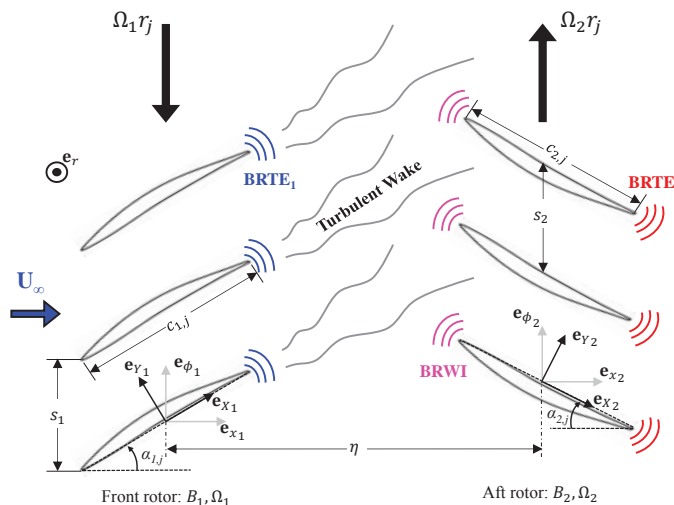

Figure 2. Illustration of broadband source mechanisms and important geometric/flow parameters on a 2D representation (r-plane slice) of a $B_1 \times B_2$ bladed CROR. Images adapted from Refs. 8, 11.

The models presented for the BRWI and BRTE source mechanisms stem from the formulation for radiation of rotating free-field noise sources by Ffowcs Williams and Hawkings,[12] and are summarized here from Ref. 8. The primary approximations that apply to both BRWI and BRTE noise models are as follows:

- The rotor blades are discretized into spanwise elements of width Δr and centered at $\bar{r}$, over which the blade geometry and flow parameters are assumed to be constant.

- The local flow behavior is assumed to be two-dimensional.

- Acoustic interactions between adjacent blades in a blade row are neglected (low rotor solidity).

- The observer is assumed to be in the acoustic far-field.

- Any installation effects on radiation of broadband noise are neglected.

The formulations presented in this study are for the calculation of the power spectral density (PSD) of acoustic pressure at an emission radius and polar angle (r_e, θ_e), which represent a convective amplification correction of a geometric observer position (r_o, θ_o). These locations are measured from the rotor hub center

in-line with the aft rotor pitch change axis, with θ_e being measured from the upstream direction. The aerodynamic information that is required by the formulations pertaining to the wake behavior of the rotor blade elements is computed on a blade element basis. This blade element analysis is performed using the XFOIL software, which is a panel method code for the inviscid or viscous analysis of isolated airfoils in subsonic steady flows.[13]

A.   Broadband Rotor Wake Interaction Noise

The method of CROR BRWI noise prediction is emulated from that derived by Blandeau[10] and Blandeau et al.[8] It stems from a time-domain representation of the pressure jump across the rear rotor blades due to incoming turbulence, which is converted to observer time and spatial coordinates, then Fourier transformed. The expression for the PSD of far-field pressure for the BRWI source mechanism of the jth spanwise blade element is

$$
S_{pp,j}^{\mathrm{BRWI}}\left(r_e, \theta_e, \omega\right) = \quad \frac{\pi}{2}\left[\frac{B_1 \rho_0 k_0 b_{2,j}}{r_e\left(1 - M_x \cos\theta_e\right)}\right]^2 B_2 U_{X2,j} \sum_{l=-\infty}^{\infty} \sum_{m=-\infty}^{\infty} \Phi_{ww}\left(0, K_{X,j,ml}\right)\left|\mathcal{L}^{\mathrm{LE}}\left(0, K_{X2,j,l}, \kappa_{2,j,l}\right)\right|^2
$$

$$
\int_{\bar{r}_j-\frac{\Delta r}{2}}^{\bar{r}_j+\frac{\Delta r}{2}} f_m^2\left(\alpha_{1,j}, r_j\right) J_l^2\left(\frac{k_0 r_j \sin\theta_e}{1 - M_x \cos\theta_e}\right)\left(\frac{l}{k_0 r_j}\cos\alpha_{2,j} - \frac{\cos\theta_e \sin\alpha_{2,j}}{1 - M_x \cos\theta_e}\right)^2 dr_j. \tag{1}
$$

Equation 1 represents a simplified expression developed by Blandeau[10] capitalizing on the assumption of there being no correlation between the unsteady loading of the blades on the aft rotor. This has been found by Blandeau et al.[8] to be an acceptable simplification for CROR configurations in which

$$
\frac{2 b_{W,j}}{s_2} < 1, \tag{2}
$$

where $b_{W,j}$ represents the half-width of the wake generated by the jth front rotor blade element. This "wake criterion" simply states that the width of the wake generated by a front rotor blade element must be smaller than the linear separation distance between the blade elements of neighboring aft rotor blades.

One of the most important underlying assumptions incorporated in this formulation is that the wake turbulence is isotropic, which is accounted for by the wavenumber spectrum Φ_{ww}. Two common models of isotropic turbulence are the Von Kármán and Liepmann models,[14,15] the latter of which is used in this study. This model was chosen because it models higher frequency behavior that is more representative of that observed in the experimental data. The simplified two-dimensional turbulent velocity spectra for the Liepmann turbulence model is

$$
\Phi_{ww,\mathrm{L}}\left(0, k_X\right) = \frac{3\overline{w^2}}{4\pi} L^2 \frac{L^2 k_X^2}{\left(1 + L^2 k_X^2\right)^{5/2}}, \tag{3}
$$

where L represents the turbulent integral length scale and $\overline{w^2}$ is the mean square velocity of wake turbulence. The unsteady loading term $\left|\mathcal{L}^{\mathrm{LE}}\left(0, K_{X,l}, \kappa_l\right)\right|^2$ is given by

$$
\left|\mathcal{L}^{\mathrm{LE}}\left(0, K_{X,l}, \kappa_l\right)\right|^2 = \frac{1}{b_2^2}\left|\int_{-b_2}^{b_2} g^{\mathrm{LE}}\left(X_2, 0, K_{X,l}, M_{X2}\right) e^{-j\kappa_l X_2} dX_2\right|^2, \tag{4}
$$

where $b_2 = c_2/2$ is the half-chord length of the aft rotor blade element and g^{LE} is the flat-plate response function due to leading edge interactions, which is computed using the model derived by Amiet.[16] Furthermore, the Fourier components of the mean wake profile are given by

$$
f_m\left(\alpha_1, r\right) = \frac{1}{B_1 \sigma \sqrt{2\pi}} \exp\left[-\frac{1}{2}\left(\frac{m}{\sigma}\right)^2\right], \tag{5}
$$

where $\sigma = r \cos\alpha_1 \sqrt{2\ln 2}/B_1 b_W$. It is worth noting that Eq. 5 implies a Gaussian turbulent wake profile, which in turn assumes that the turbulence of interest is generated on the blades and is negligible elsewhere.

American Institute of Aeronautics and Astronautics

Finally, the turbulence wavenumbers $K_{X,j,ml}$ and $K_{Xi,j,l}$, and aeroacoustic coupling wavenumber $\kappa_{i,j,l}$ are respectively defined as

$$K_{X,j,ml} = \frac{\omega - l\Omega_2 + mB_1(\Omega_1 + \Omega_2)}{U_{X2,j}}, \quad K_{Xi,j,l} = \frac{\omega - l\Omega_i}{U_{Xi,j}}, \tag{6}$$

and

$$\kappa_{i,j,l} = \frac{l}{\bar{r}_j}\sin\alpha_{i,j} + \frac{k_0 \cos\alpha_{i,j} \cos\theta_e}{1 - M_x \cos\theta_e}. \tag{7}$$

In addition to the terms mathematically defined here, other terms pertaining to the wake behavior of the blade elements (such as b_W, L, $\overline{w^2}$) are computed using the relations presented in Blandeau et al.[8] These are summarized in Section C.

B.   Broadband Rotor Trailing Edge Noise

The expression used in this study for the PSD of far-field pressure for the BRTE source mechanism of the jth spanwise blade element of the ith rotor is

$$S_{pp,j}^{\mathrm{BRTE}_i}(r_e, \theta_e, \omega) = \frac{B_i}{8\pi}\left[\frac{k_0 b_{i,j}}{r_e(1 - M_x\cos\theta_e)}\right]^2 \sum_{l=-\infty}^{\infty} S_{qq}(0, K_{X,l,i,j})\left|\mathcal{L}^{\mathrm{TE}}(0, K_{Xi,j,l}, \kappa_{i,j,l})\right|^2$$

$$\int_{\bar{r}_j - \frac{\Delta r}{2}}^{\bar{r}_j + \frac{\Delta r}{2}} J_l^2\left(\frac{k_0 r_j \sin\theta_e}{1 - M_x\cos\theta_e}\right)\left(\frac{l}{k_0 r_j}\cos\alpha_{i,j} - \frac{\cos\theta_e \sin\alpha_{i,j}}{1 - M_x\cos\theta_e}\right)^2 dr_j. \tag{8}$$

Note that Eq. 8, which was also developed by Blandeau[10] and Blandeau et al.,[8] capitalizes on the assumption of there being no correlation between adjacent rotor blade source elements. The wavenumber surface pressure cross-spectrum is further defined as

$$S_{qq}(0, k_x) = \frac{1}{\pi}l_r(k_X U_c)\Phi_{pp}(k_X U_c), \tag{9}$$

where $\Phi_{pp}(\omega)$ is the surface pressure spectrum near the trailing edge, l_r is the spanwise correlation length, and U_c is the eddy convection velocity. For this study, $\Phi_{pp}(\omega)$ is computed using the model of Kim and George.[17] This empirical relation requires knowledge of the boundary layer displacement thickness δ_i^* near the trailing edge, which is computed using XFOIL for a subset of blade elements along the span of each rotor blade. Finally, the trailing edge interaction unsteady loading term for an arbitrary (i,j)th rotor blade element is formulated similar to the leading edge one presented in the previous section as

$$\left|\mathcal{L}^{\mathrm{TE}}(0, K_{X,l}, \kappa_l)\right|^2 = \frac{1}{b^2}\left|\int_{-b}^{b} g^{\mathrm{TE}}(X, 0, K_{X,l}, U_c)e^{-j\kappa_l X}dX\right|^2, \tag{10}$$

where g^{TE} is the flat-plate response function due to trailing edge interaction formulated by Roger and Moreau.[18]

C.   Estimates of Flow and Wake Parameters

The formulations presented thus far have several key parameters that must be determined empirically. For BRWI noise, these include the component of total velocity aligned with the aft blade chord, $U_{X2,j} = U_{2\mathrm{res},j}\cos(AoA_{2,j})$, the wake half-width generated by the front rotor blade, $b_{W,j}$, the integral turbulent length scale, L, and the mean square velocity of wake turbulence, $\overline{w^2}$. The aft rotor relative velocity is a function of the induced velocities that are the result of the thrust generated by the rotor blades, the rotational velocities of the blades themselves, and the induced tangential velocity generated in the wake of the front rotor. This is estimated using conventional rotor momentum and blade element theories, which are discussed in Section IV. The turbulent length scale is assumed to be directly related to the wake half-width according to the relation identified by Jurdic et al.,[19]

$$L = 0.42b_W. \tag{11}$$

The wake half-width is further defined according the hot-wire measurements made in the near-wake of a fan blade[20] as

$$\frac{b_W}{\theta_{\mathrm{MT},1}} = \sqrt{0.158X_\Theta + 2.494}, \tag{12}$$

where $\theta_{\mathrm{MT},1} = C_d b_1$ is the momentum thickness of the front blade element and $X_\Theta = X_\eta/2\theta_{\mathrm{MT},1}$. Finally, the mean square fluctuating wake velocity is modeled in a manner similar to that of Blandeau et al.,[8] consisting of a twelfth-order polynomial curve fit to the near-wake total maximum turbulence velocity data of Gliebe et al.[20]

$$\frac{\sqrt{\overline{w^2}}}{u_0} = 0.00452X_\Theta + 0.3553, \quad \text{for } X_\Theta < 65, \tag{13}$$

and the far-wake data for a symmetric airfoil of Wygnanski et al.[21] Note that the centerline velocity defect, u_0 is also modeled using the following relation of Gliebe et al.:[20]

$$\frac{U_{X1}}{u_0} = \sqrt{2.133X_\Theta + 7.458}. \tag{14}$$

It is important to note that Eqs. 11 - 14 are all dependent on the blade sectional drag coefficient, C_d. As will be seen in Section V, this parameter plays an important role in determining the spectral amplitude at peak frequency for BRWI noise.

The spectral behavior of the BRTE noise model investigated here is determined by the wavenumber cross-spectrum of Eq. 9, the primary parameters of which are the blade spanwise correlation length, l_r, and the blade boundary layer displacement thickness, δ^*. The correlation length is defined in a piecewise manner according to the findings of Rozenberg et al.[22] as a modification to the traditional model of Corcos:[23]

$$l_r\left(\omega\right) = \frac{b_c U_c}{\omega}, \tag{15}$$

where

$$b_c = \left\{ \begin{array}{ll} 1.56 & \text{for } r/R_i \leq 0.85 \\ 0.90 & \text{for } r/R_i > 0.85 \end{array} \right\}. \tag{16}$$

This estimate of the correlation length capitalizes on the assumption that the turbulence is "frozen," meaning that turbulence is simply convected by the local mean flow. The eddy convection velocity is set as $U_c = 0.6U_X$ according to the findings of Brooks and Hodgson.[24]

III. The F31/A31 Blade Configuration

The F31/A31 historical baseline CROR configuration[6,25] is examined in this study. Products of the late 1980s, these blades were primarily designed based on aerodynamic performance optimization. Acoustic performance was not one of the primary drivers in the design. Figure 3 presents a rendered profile view of the F31/A31 blades. In this section, the blade design parameters and investigated flow conditions are discussed.

A. Blade Geometries

The blade element profiles used in the broadband analysis are extracted in spanwise (radial) slices. A total of 50 evenly-spaced slices are extracted per blade, a subset of which are selected for input into the broadband noise formulations. The primary geometric parameters of interest are the chord lengths c_i and the blade stagger angles α_i. However, in addition to the orientation of the blades, the blade shapes themselves also require consideration. Previous implementations of the broadband formulations discussed in Section II by Blandeau et al.[8] used NACA 0012 profiles for the rotor blade elements. Because the F31/A31 blades are asymmetric and have thin profiles, a different method is used here to account for the blade section element geometries. In the current study, each spanwise blade element is replaced with a NACA 4-digit airfoil of similar thickness and camber for aerodynamic analysis using the XFOIL software. While this technique was found to yield reasonable comparisons between the majority of the F31/A31 blade shapes and their corresponding NACA replacement profiles, some modifications were made to the replacement profiles in the vicinity of 70% tip radius. This is because the relatively high angles of attack experienced by the rotor blades near this spanwise location required an increase in the maximum thickness of the blade elements in order to achieve a converged solution in XFOIL.
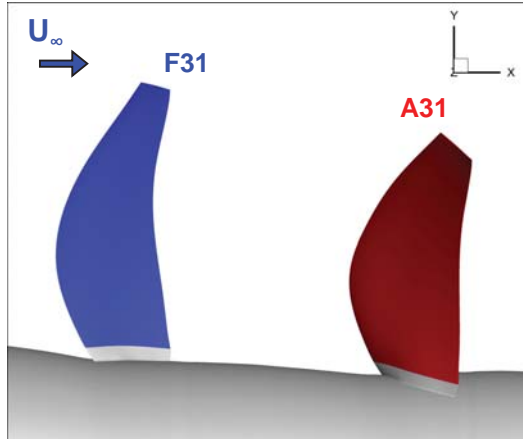
Figure 3. Rendered in-situ view of the F31/A31 historical baseline blades.

B. Flight Conditions

The flight conditions investigated in this study are representative of aircraft approach and take-off conditions. Acoustic experiments were performed on the F31/A31 blade set in the NASA 9×15 wind tunnel at NASA Glenn Research Center (see Fig. 1(a)). The isolated CROR apparatus was subjected to a freestream Mach number of $M_\infty = 0.2$ and run across a wide range of rotor speeds (RPMs). A total of five rotor speeds are investigated here, four of which represent a take-off blade pitch condition. The fifth speed is indicative of a nominal approach blade pitch condition with a mid-range RPM. A summary of the F31/A31 primary design parameters and investigated flight conditions is presented in Table 1. Note that the rotor RPMs highlighted in **bold** represent those that were investigated using unsteady Reynolds-averaged Navier Stokes (u-RANS) CFD. The CFD runs are performed for the purpose of verifying the aerodynamic trends modeled using rotorcraft blade element-momentum theory. Because the intermediate rotor speeds ($\Omega_i = 5589, 6068$ RPM) do not have supporting CFD data associated with them, the broadband noise predictions for these cases use the aerodynamic input trends extracted from the other cases. This is meant to serve as a validation of the generalized method of aerodynamic input extraction for prediction of broadband noise for an arbitrary CROR flight case.

Table 1. Design parameters and flight conditions of the F31/A31 blade set considered in this study.

Parameter	F31	A31
Number of Blades (B_i)	12	10
Tip Radius,* m	0.327	0.315
Design Tip Speed,** m/s	228.6	220.2
Rotor Speed (Ω_i), RPM	**4620**	**4620**[†]
	5551	**5551**[†]
	5589	5589[‡]
	6068	6068[†]
	6436	**6436**[†]
Blade Stagger Angle (α),*** deg.	49.9	49.2[†]
	56.5	54.3[‡]

*Model-scale

**Take-off values

***Value at 75% tip radius, rel. to axial direction

[†]Take-off configuration

[‡]Approach configuration

American Institute of Aeronautics and Astronautics

IV. Analysis of In-Flow Conditions

Blade element loading analysis[26] can be used to estimate the flow − both axially and tangentially − through the front rotor disk. This information in turn may be used to approximate the in-flow conditions experienced by the aft rotor disk. As will be seen, implementation of blade element analysis using XFOIL generally results in an over-prediction of the loads when compared with those computed via CFD as well as from experiments. This is believed to be the direct result of applying a two-dimensional analysis for a highly three-dimensional problem. It will also be seen that application of a scale factor to the force data computed in XFOIL yields blade loads, and thus in-flow velocities that closely resemble the trends exhibited by the CFD data.

A. Actuator Disk and Blade Element Analyses

Definition of the CROR in-flow conditions is important because they directly affect the angles of attack and relative velocities experienced by the rotor blades. A schematic of illustrating the two-dimensional aerodynamics of a CROR blade element is presented in Fig. 4. It is important to note that the coordinate system in this figure represents that of the local blade element, rather than the global one presented in Fig. 2. The general definitions of the resultant velocity and angle of attack at a radial station r for a rotating blade are respectively

$$U_{\text{res}}(r) = \sqrt{(\Omega r)^2 + U_x^2} \tag{17}$$

and

$$AoA(r) = \tan^{-1}\left(\frac{\Omega r}{U_x}\right) - \alpha. \tag{18}$$

Use of actuator disk theory (ADT)[27] can also provide a crude estimate of the net induced velocity at the rotor "disk" as

$$U_{x,\text{ADT}} = \frac{U_\infty}{2} + \sqrt{u_{I,\text{ADT}}^2 + \left(\frac{U_\infty}{2}\right)^2}, \tag{19}$$

where $u_{I,\text{ADT}} = \sqrt{\frac{T}{2\rho_0 A}}$ is the induced velocity, T is the thrust generated by the rotor, and $A = \pi\left(R^2 - r_{\text{hub}}^2\right)$ is the area of the rotor disk. This equation is limited in two important ways: it requires knowledge of the rotor thrust, and it provides only a single data point to represent the axial velocity increase for the entire disk area. It is also important to consider the tangential, (or "swirl") component of velocity induced by the front rotor as it could have drastic effects on the effective angles of attack experienced by the aft rotor blades.

It is useful to define the in-flow velocities in terms of conventional rotorcraft non-dimensional parameters. The axial velocity can be defined in terms of an in-flow ratio, λ, as

$$\lambda(r) = \lambda_\infty + \lambda_I(r) = \frac{U_\infty}{\Omega R} + \frac{u_I(r)}{\Omega R}, \tag{20}$$

while the tangential velocity can be defined in terms of an induced swirl coefficient, Θ, as

$$\Theta(r) = \frac{u_\theta(r)}{\Omega r}, \tag{21}$$

where $u_I(r)$ and $u_\theta(r)$ are the induced axial and tangential velocities at a radial station r. These are the unknown quantities that are needed to characterize the two-dimensional in-flow conditions experienced by the blade element. The induced axial in-flow velocity can be solved for using combined rotorcraft blade element and momentum theories,[26] while the swirl
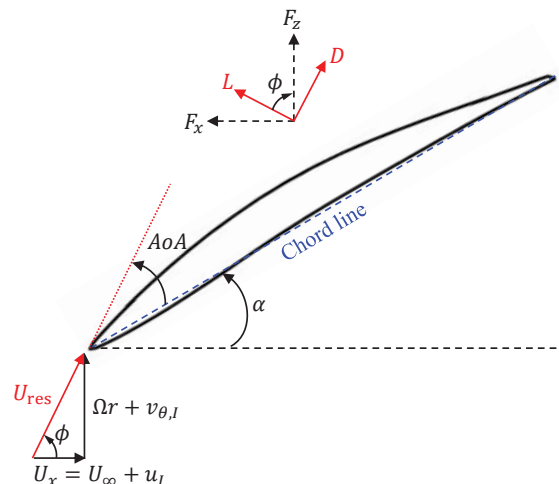
Figure 4. CROR two-dimensional blade element aerodynamics.

coefficient can be solved for using the aerodynamic model of Ref. 28. Both of these techniques require knowledge of the lift and drag forces on the blade sections. From the differential form of momentum theory,[26] the differential thrust coefficient on an annulus of the rotor disk at radial station r of width Δr is

$$dC_T = \frac{dT}{\rho A \left(\Omega R\right)^2} = 4\lambda\lambda_I r \Delta r, \tag{22}$$

where dT is the differential thrust at the radial station and $A = \pi R^2$ is the total disk area. Furthermore, the swirl coefficient can be defined as

$$\Theta = \frac{C_l \sigma U_{\text{res}}}{2\Omega r} \tag{23}$$

where $\sigma = cB/2\pi r$ is the rotor solidity at radial station r. The differential thrust, torque, and power can also be solved for from a blade element perspective using

$$dT = BF_x\Delta r, \tag{24}$$

$$dQ = BF_z r\Delta r, \tag{25}$$

$$dP = BF_z\Omega r\Delta r, \tag{26}$$

where

$$F_x = L\sin\phi - D\cos\phi = \frac{1}{2}\rho U_{\text{res}}^2 c \left(C_l\sin\phi - C_d\cos\phi\right) \tag{27}$$

and

$$F_z = L\cos\phi + D\sin\phi = \frac{1}{2}\rho U_{\text{res}}^2 c \left(C_l\cos\phi + C_d\sin\phi\right). \tag{28}$$

In this study, the differential loading information is extracted in two possible ways: directly from the CFD results, and/or via two-dimensional blade element analysis (BEA) using the XFOIL software. The latter of these methods provides force coefficient information (C_l, C_d), that can be input into Eqs. 23, 27, and 28. Unfortunately, it has been found that the blade element analysis aforementioned cannot be used to determine the in-flow velocity upstream of the front rotor disk. This is because the velocity field upstream of the front rotor is due to a combination of the boundary layer flow over the rotor hub and upstream influence of the rotor blades. Because the blade element analysis accounts for the forces encountered by the rotor blades, it is believed to be a reasonable method for predicting the flow behavior between the front and aft rotor, in an azimuthally-averaged sense. This technique is described in Section C.

B.   CFD In-Flow Conditions

To get a more comprehensive look at the induced velocities experienced by a CROR, CFD results are consulted. A visual representation of the axial in-flow ratio and swirl coefficient at planes immediately upstream of the front and aft rotors is presented in Fig. 5. The data represents a single time step of an OVERFLOW2[29, 30] CFD simulation of the F31/A31 CROR configuration for $\Omega_1 = \Omega_2 = 6436$ RPM and a freestream Mach number of $M_\infty = 0.2$. As the results show, the front rotor experiences a gradual decay in axial induced velocity with increase in radial distance from the rotor hub, with negligible induced swirl velocity. The aft rotor disk, however, displays azimuthal periodicity in both axial and tangential velocities due to the wakes generated by the front rotor blades.

While Fig. 5 provides a detailed view of the flow behavior across the rotor disks, the blade element analysis used in this study calls for a mean input velocity profile as a function of span along the rotor blade. This is accomplished by averaging the CFD data azimuthally. The results of the azimuthally-averaged in-flow ratios immediately upstream of the front rotor disk are shown in Figs. 6 for the three simulated rotor RPMs. In addition, this figure displays the single in-flow ratio data points computed using ADT plotted at 75% tip radius (approximately half of the blade span), which are computed as $\lambda_{\text{ADT}} = U_{x,\text{ADT}}/\Omega R$ and $U_{x,\text{ADT}}$ is from Eq. 19. As the figure also shows, the axial velocity decays linearly as a function of increasing distance from the rotor hub, with the exception of the region close to the hub itself. This region shows a drastic decrease in axial velocity as a result of boundary layer development along the hub surface. If attention is focused on the linear portion of the in-flow profiles for the different rotor speeds, they are seen to be nearly

parallel. Linear curve fits were computed for these profiles using a common starting radial index (denoted by the vertical dotted line in Fig. 6), the slopes and y-intercept values of which are provided. The lowest determination coefficient (r-squared value) for these curves was 0.9973. While the slopes are seen to slightly increase in magnitude with rotor RPM, this increase is considered to be rather small compared to the wide range of represented RPMs. Therefore, an average of these slope values was computed. An additional linear curve fit was computed for the three y-intercept values by plotting them as a function of ADT induced in-flow ratio, or $\lambda_{I,\text{ADT}} = u_{I,\text{ADT}}/\Omega R$. This yielded a determination coefficient of 0.9983. The resulting generalized model for the in-flow velocity for the front rotor is

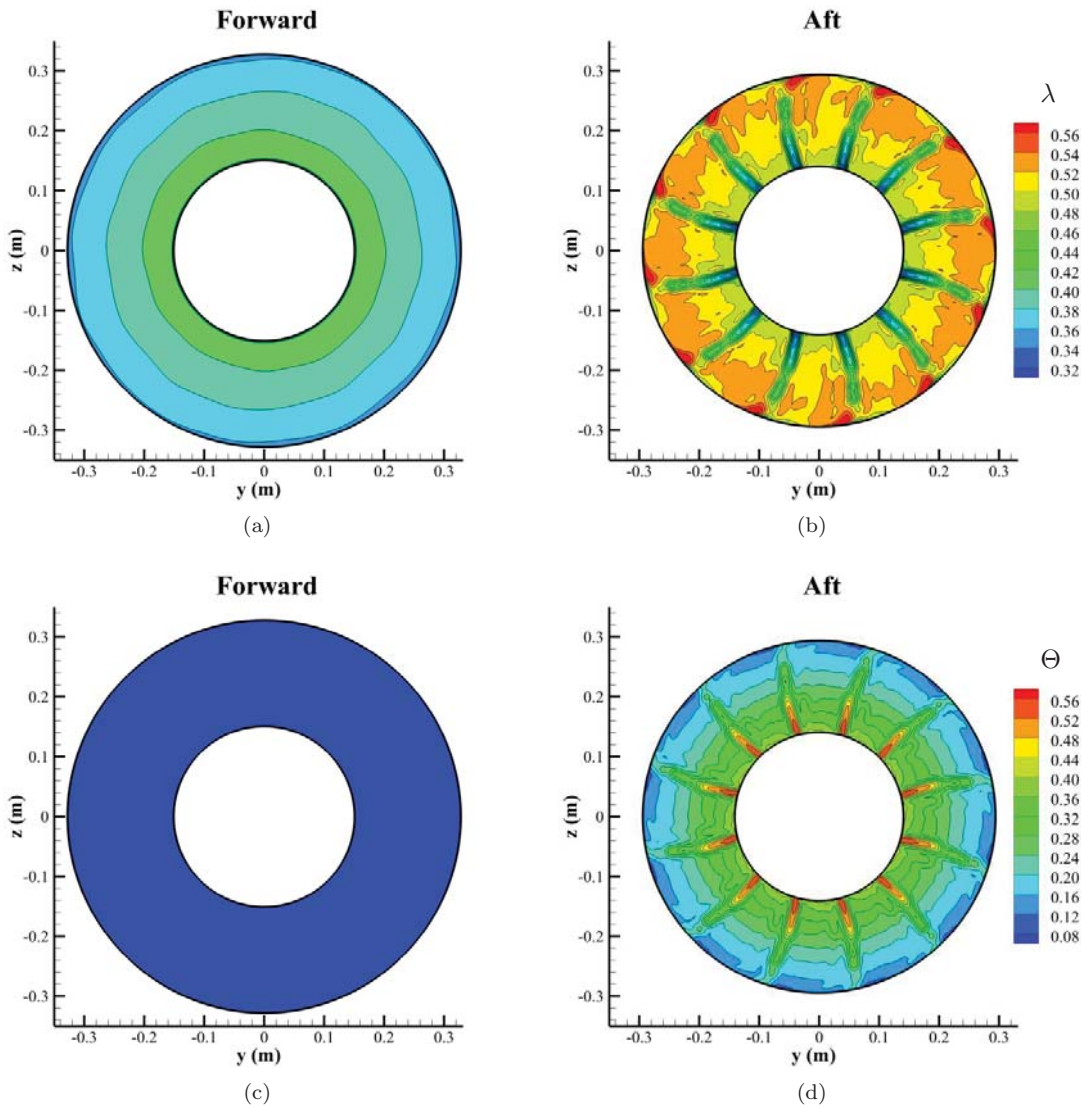$$\lambda_{\text{model}}(r) = -0.0958\frac{r}{R_1} - 1.7889\lambda_{I,\text{ADT}} + 0.835. \tag{29}$$

Figure 5. Contours of (a), (b) axial in-flow ratio and (c), (d) swirl coefficient immediately upstream of front rotor (left column) and aft rotor (right column). Results are for the case of $\Omega_i = 6436$ RPM.

C. Induced Velocities from Blade Element Forces

As was stated in Section II, the relative blade section velocities $U_{Xi} = U_{\text{res},i}\cos(AoA_i)$ are important scaling parameters for the broadband noise predictions. In the previous section, simple linear curve fits were

American Institute of Aeronautics and Astronautics
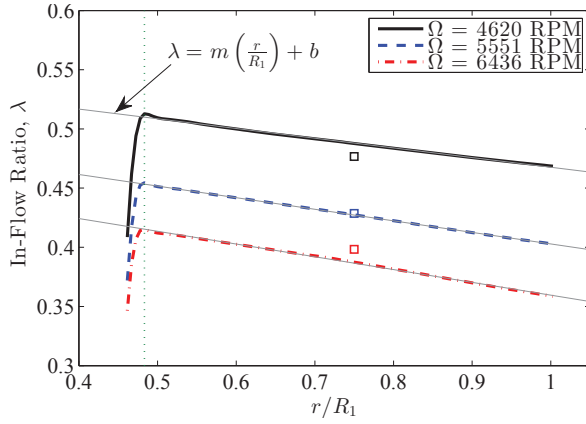
Figure 6. Azimuthally averaged in-flow ratio upstream of front rotor disk for three CFD cases with tabularized linear curve fit coefficients. The □ symbols represent the in-flow ratio values computed using ADT.

developed for the spanwise axial in-flow distribution for the front rotor blades. Coupling this information with the rotational velocity of the rotor blade segments ($v_\theta = \Omega r$) is considered to be sufficient for defining the two-dimensional resultant velocity vector for the front rotor. This is because there is negligible induced tangential velocity upstream of the front rotor disk. However, the interaction region between the front and aft rotors requires additional analysis.

The induced axial and tangential velocities experienced by the aft rotor blades are estimated using coupled blade element and differential momentum theories on the front rotor blades. First, the axial in-flow distribution is computed by rearranging the differential thrust coefficient expression of Eq. 22 and solving for the positive root of the following expression:

$$\lambda_{I,2}^2 + \lambda_{\text{ADT},1}\lambda_{I,2} - \frac{dC_{T,1}}{4r\Delta r} = 0, \tag{30}$$

where $\lambda_{\text{ADT},1}$ is computed using the net induced velocity from the front rotor disk (Eq. 19). Note that the subscripts $\{1, 2\}$ in Eq. 30 represent quantities applicable to the front and aft rotor disks, respectively. The resulting net induced velocity experienced by the aft rotor disk is then estimated as

$$\lambda_2 = \lambda_{\text{ADT},1} + \lambda_{I,2}. \tag{31}$$

Similarly, the swirl coefficient that is meant to represent the tangential velocity generated by the front rotor disk is rewritten from Eq. 23 as

$$\Theta_2 = \left\{ \frac{C_l \sigma U_{\text{res}}}{2\Omega r} \right\}_1. \tag{32}$$

Finally, the results of Eqs. 31 and 32 can be substituted respectively into Eqs. 20 and 21 to obtain the dimensional axial and swirl velocities experienced by the aft rotor.

To test how well Eqs. 31 and 32 perform at reproducing the aft rotor in-flow conditions, the CFD flow field is consulted. As before in Section B, the flow field results immediately upstream of the aft rotor blades are azimuthally averaged. Furthermore, the thrust generated by the front rotor blades are extracted from the CFD results and re-computed on a blade element basis. This is done by discretizing the blade CFD grid "zones" into spanwise sections that match those analyzed in XFOIL, and summing the load contributions enclosed by the appropriate blade element. An illustration of this conversion is presented in Fig. 7 for the case of $\Omega_i = 6436$ RPM. This further allows direct comparison of the loads and in-flow velocities between the CFD and XFOIL blade element results.

Comparisons of the differential thrust coefficient, swirl coefficient, and in-flow ratio between the CFD and blade element
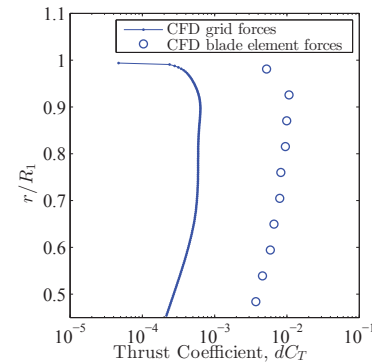

Figure 7. Blade element representation of differential thrust coefficient of front rotor computed from CFD grid ($\Omega = 6436$ RPM).

American Institute of Aeronautics and Astronautics

results are provided in Fig. 8. Note that the blade element analysis results shown in this figure were computed using the in-flow velocity model of Eq. 29. If attention is paid to Fig. 8(a), a noticeable discrepancy can be observed between the blade element thrust values computed from CFD and those computed in XFOIL. This is believed to be due to the fact that a two-dimensional flow solver such as XFOIL cannot account for losses due to three-dimensional effects. To remedy this discrepancy, the differential thrust coefficients are scaled by the ratio of total thrust computed by CFD over that computed by blade element theory. It is worth noting that a similar scaling procedure was performed based on shaft horsepower for the rotor differential power coefficient in Ref. 28. The scaled XFOIL results are seen to line up very well with the CFD ones in Fig. 8(a) for the majority of the blade span, with the largest discrepancies occurring near the blade tip. Despite this, however, the trends between the two line up very well. Applying this thrust ratio scaling factor to dC_T and C_l in Eqs. 30 and 32 yield the scaled blade element results of Figs. 8(b) and 8(c), respectively. The results show overall reasonable comparisons with the CFD azimuthally averaged flow field. An interesting observation to be made from the CFD results is the presence of a drastic decrease in in-flow ratio and increase in swirl around 95% blade span. This is indicative of the downstream convection of the tip vortex generated by the front rotor blades. Because this blade element method is traditionally meant to approximate the flow behavior at the rotor "disk," it is unable to account for a complex flow feature such as the tip vortex. It is also worth noting that Fig. 8 represents the worst case results for these comparisons out of the three simulated cases. Based on these results, it appears that using the scaled XFOIL blade element loads effectively captures the overall in-flow and swirl velocity trends upstream of the aft rotor disk.
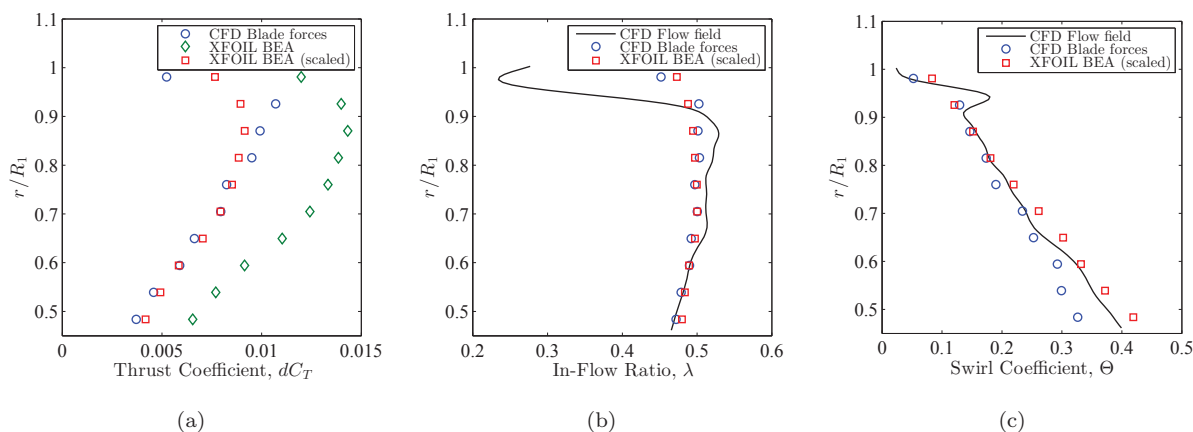
Figure 8. Front rotor blade element results for $\Omega = 6436$ RPM: (a) differential thrust coefficient, (b) in-flow ratio, and (c) swirl coefficient. CFD flow field data averaged azimuthally at an axial location directly upstream of aft rotor. Scaling of XFOIL results based on ratio of rotor thrusts.

It is also important to analyze the effects of the different in-flow conditions on the parameters input into the blade element analysis using XFOIL. These are the total velocity, U_{res}, and the angle of attack, AoA, which is measured perpendicular to the pitch change axis in the plane of the blade section in question. Figure 9 displays these parameters for three different prescribed in-flow conditions: (1) those computed from the combination of ADT and blade element analysis (ADT-BEA), (2) those computed from using the in-flow model of Eq. 29 coupled with BEA ($\lambda_{\mathrm{model}} - $ BEA), and (3) those extracted from the azimuthally-averaged CFD data. Note that the first condition consists of only the single data point of induced axial velocity from ADT applied to the entire span of the front and aft rotor disks (Eq. 19), while the second condition utilizes the in-flow model of Eq. 29 for the front rotor and Eqs. 30 and 31 for the aft rotor. Both of these conditions utilize Eq. 32 for computing the swirl velocity encountered by the aft rotor based on the blade element results of the front rotor. The front rotor results of Fig. 9(a) and 9(b) show small differences in both velocity and angle of attack for all three models, however the in-flow model (2) compares slightly better with the CFD. The largest discrepancies between the CFD in-flow and the ADT-BEA data sets occur near the hub and tip of the rotor blade. If attention is focused on the aft rotor blade results, it can be seen that there are larger discrepancies between the two models and the CFD data set, namely near the tip of the rotor blade. This is due to the downstream convection of the front rotor tip vortex, which is not accounted for in the empirical models. Figure 9(d) shows, however, that the in-flow trend model yields better agreement in aft rotor angles of attack with the CFD in-flow data than the ADT-BEA one does.
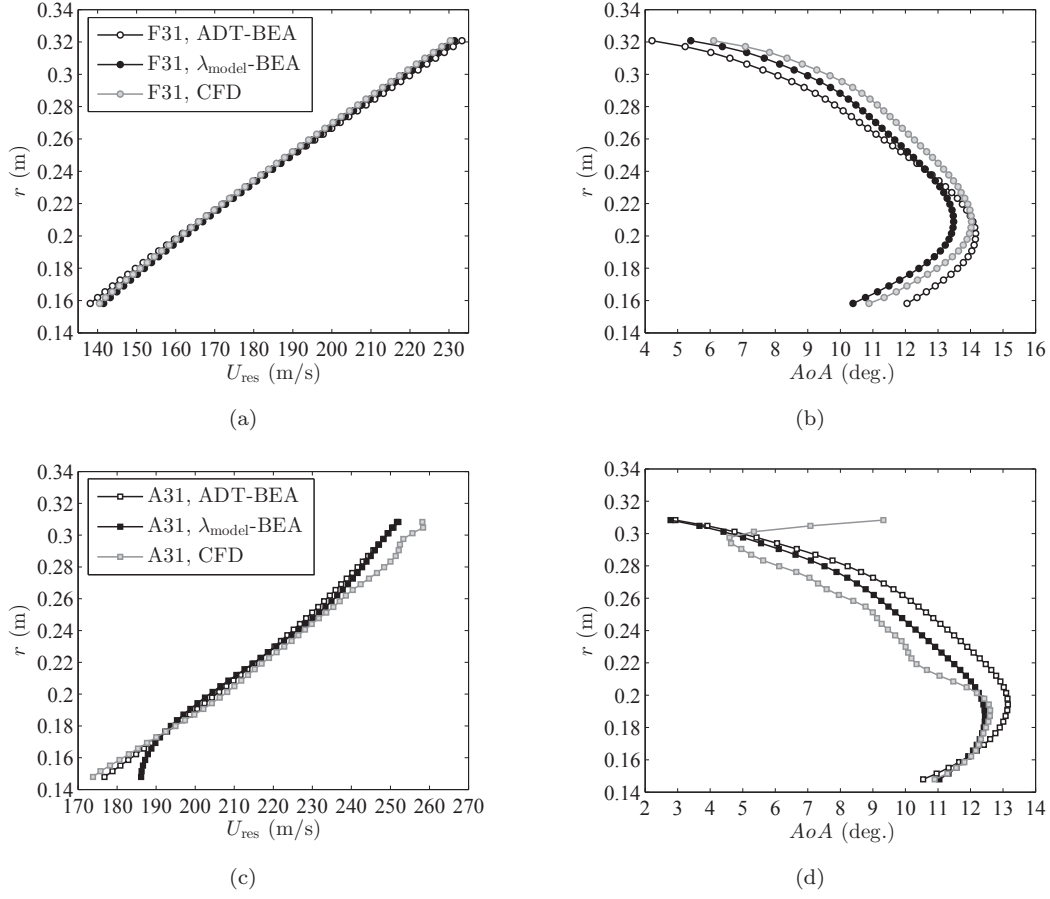
Figure 9. Input flow parameters for blade element analysis of front (top) and aft (bottom) rotor blades subjected to different in-flow conditions: (a), (c) resultant velocities, and (b), (d) angles of attack. Data presented is for the case of $\Omega = 6436$ RPM.

A total of ten, linearly spaced blade elements are analyzed on both the front and aft rotor blades using XFOIL. As was discussed in Section C, the parameters computed from the blade element analysis that impact the BRWI and BRTE noise predictions are the drag coefficients of the front rotor blade elements and the trailing edge displacement thicknesses of both front and aft rotor blade elements, respectively. Figure 10 shows these parameters for the case of $\Omega = 6436$ RPM. Note that only the suction side displacement thicknesses are shown because they are considerably larger in amplitude as compared to those on the pressure sides of the blade elements, and thus contribute more prominently to the broadband noise. If attention is focused on Figs. 10(a) and 10(b), very similar trends in C_d and δ_s^* for the front rotor blade can be observed. While these trends are very similar between the two modeled in-flow conditions, the CFD in-flow condition consistently displays higher values of C_d and δ_s^* for $r/R_1 > 0.70$. Figure 10(c) shows suction side displacement thicknesses at the trailing edge of the aft rotor that are comparable to those computed for the front rotor. It is also interesting to note the drastic increase in $\delta_{s,2}^*$ near the tip of the aft rotor blade for the CFD in-flow condition, which is directly related to the increase in angle of attack at this location (see Fig. 9(d)).

V.   Broadband Spectral Predictions

The BRWI and BRTE formulations presented in Section II are computed and compared with experimental acoustic PSD data acquired in the 9×15 Low Speed Wind Tunnel (LSWT) at the NASA Glenn Research Center.[6] The experimental microphone data were acquired at a series of locations along a linear traverse (see Fig. 1(a)), which was located 1.524 m away from the rotor hub centerline. Standard corrections for atmospheric attenuation were applied to the experimental data, with the "source" region defined by the

American Institute of Aeronautics and Astronautics
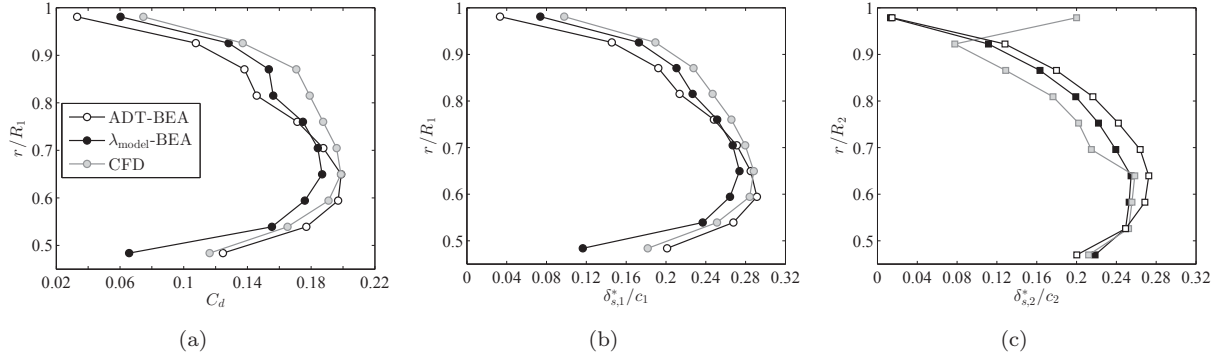
Figure 10. Output wake parameters from blade element analysis using XFOIL for different in-flow conditions: (a) drag coefficients of front rotor blade, (b) suction side displacement thicknesses at front rotor trailing edge, and (c) suction side displacement thicknesses at aft rotor trailing edge. Data presented is for the case of $\Omega = 6436$ RPM and the same in-flow conditions presented in Fig. 9.

intersection of the aft rotor pitch change axis and the rotor hub centerline. The broadband components of the experimental acoustic spectra, $B_{\text{Expt.}}$, were obtained by implementing a peak-finding algorithm on the spectra, in which any narrowband spectral value greater than 2 dB above its neighboring frequency bins was flagged as a tonal contribution. The spectral content at these frequency bins was then removed and replaced with the average spectral level of the neighboring frequency bins. The broadband predictions are computed using either the in-flow data extracted from the CFD predictions or the conditions estimated using combined ADT-BEA for comparison with the experimental data. All BRWI predictions are computed using the Liepmann model of isotropic homogeneous turbulence. All acoustic spectra presented are on a model-scale frequency basis.

A.   Effects of In-Flow Conditions

The goals of this study are to examine the use of traditional rotor blade element-momentum theories to predict the aerodynamic input conditions for CROR blades, and to show that incorporation of these input conditions to previously developed semi-analytical formulations yields reasonably accurate broadband noise predictions. "Reasonably" means that the predictions should portray the appropriate scaling behavior with various parameters such as rotor RPM, blade pitch, and directivity angle. The previous section identified reasonable similarities between both the input aerodynamic conditions and resulting wake parameters using blade element analysis for the different in-flow conditions. In this section, the variability of the noise predictions is analyzed based on these different input conditions.

Figure 11 displays the comparison between broadband predictions obtained with the in-flow conditions discussed in the previous section. As Fig. 11(a) shows, the BRWI spectral trends are very similar between the different in-flow conditions. While the CFD in-flow condition is higher in amplitude across the entire frequency range considered, the largest discrepancy with the ADT-BEA model is less than 1.5 dB at a frequency of 2.5 kHz. Furthermore, the largest difference between the ADT-BEA and λ_{model}-BEA cases is less than 0.4 dB across the entire frequency range considered. These trends can be related to the drag coefficient data presented in Fig. 10(a), in which the CFD in-flow case shows higher C_d values than the other two cases for $r/R_1 > 0.70$. The BRTE predictions of Fig. 11(b) also show very similar spectral trends between the different in-flow conditions for both the front and aft rotor trailing edges. The largest discrepancies in the predictions occur for frequencies above 20 kHz, at which point the BRTE contributions to the total noise are considerably less than the BRWI component of noise. The total noise prediction, consisting of the sum of BRWI and BRTE noise contributions, for the nominal take-off condition is shown in Fig. 11(c) for an observer angle of $\theta_o = 45°$. As this figure shows, an overall good approximation of the broadband spectral shape is obtained. It is worth noting that a slight over-prediction is evidenced for all in-flow conditions in the frequency range of $1.0 \leq f \leq 1.4$ kHz. Despite this however, all three in-flow conditions yield total noise predictions that follow the experimental broadband spectral shape rather well. While the CFD in-flow condition fits better in an overall sense, the largest discrepancy in levels between this case and the ADT-BEA case is less than 1.5 dB across the entire tested frequency range.
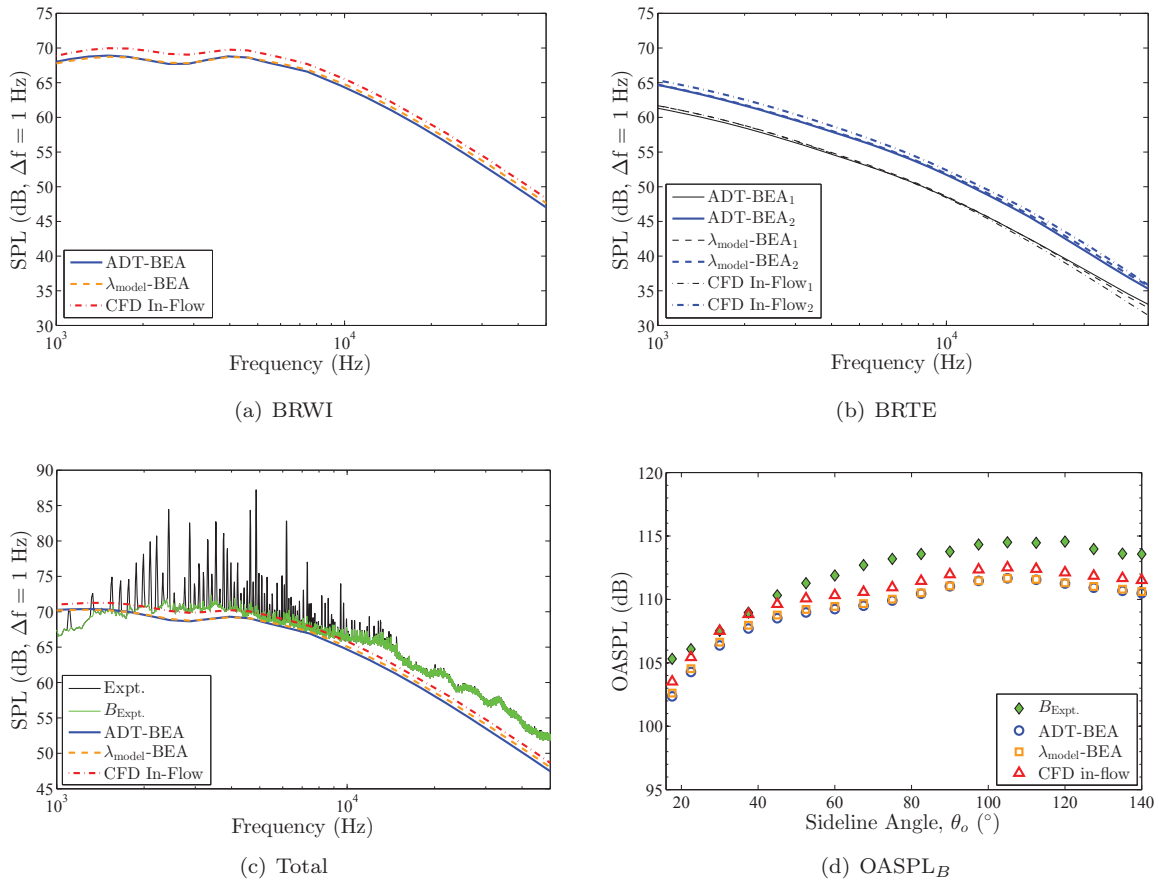
Figure 11. CROR broadband noise predictions for different in-flow conditions at $\theta_o = 45°$ for take-off condition ($\Omega = 6436$ RPM): (a) BRWI noise, (b) BRTE noise, (c) total noise with comparison to experiment, and (d) broadband OASPL comparisons.

Another metric for determining the performance of the noise predictions is overall sound pressure level (OASPL). For the experimental data, this is computed by integrating the extracted broadband component of the narrowband PSDs over the frequency range of $1.8 \leq f \leq 50$ kHz. The lower end of this frequency range is chosen for two reasons: (1) it represents an approximate cut-on frequency at which the rotor blade spanwise correlation length scale (see Eq. 15) is smaller than the width of the rotor blade elements, and (2) it represents an experimental SNR of at least 6 dB for all observation angles. In addition, frequencies above 50 kHz are not included in the analysis because they display anomalous behavior believed not to represent the physical problem under investigation. Because the predictions are originally computed on a logarithmically-spaced frequency basis, they are linearly interpolated and undergo the same integration process as the experimental data. Note that the predictions were also performed on a linearly-spaced frequency basis for several observer locations, yielding broadband OASPLs that differed from the interpolated scheme by a maximum of only 0.27 dB. Therefore, interpolation of the logarithmically-spaced broadband predictions is considered to be a reasonably accurate method of estimating the broadband OASPL. Figure 11(d) displays the broadband OASPL predictions for the different in-flow conditions with comparison to the experiment. These results show an overall under-prediction for all in-flow conditions, with the CFD in-flow dataset performing the best. The largest discrepancy between the experiment and CFD in-flow prediction is 2.5 dB. This maximum difference increases to 3.4 dB between the experiment and ADT-BEA model. All three predictions show directivity trends that are in reasonable agreement with the experiment.

B. Directivity Performance of an Intermediate Flight Condition

The broadband predictions are now carried out for an intermediate flight condition in which no supporting CFD data is available. Figure 12 displays broadband predictions for the case of $\Omega = 6068$ RPM across the range of experimentally-measured observer angles in approximately 15° increments. The predictions show overall very good agreement with the broadband experimental trends. As observed in the previous section, a slight over-prediction is seen to occur at low frequencies for a majority of the observer angles. This is again possibly related to the fact that the rotor blade spanwise correlation length scales become larger than the width of the rotor blade elements below approximately 1.8 kHz based on Eqs. 15 and 16. Usage of the current Φ_{pp} model[17] for BRTE noise could also be a source of error. This is because the F31/A31 blade geometries are considerably different from that of a NACA 0012 airfoil, the latter of which is the basis of this model. The predictions also seem to under-predict the experimental measurements over an observer angle range of $60° \leq \theta_o \leq 90°$, at high frequencies. This could be due to a number of reasons, including the possible presence of a broadband noise source not accounted for in this study, such as turbulent vortex interaction noise. While this source mechanism is similar to the BRWI component of noise, it can have a turbulence spectrum considerably different from that of an isotropic homogeneous turbulence model.[31]
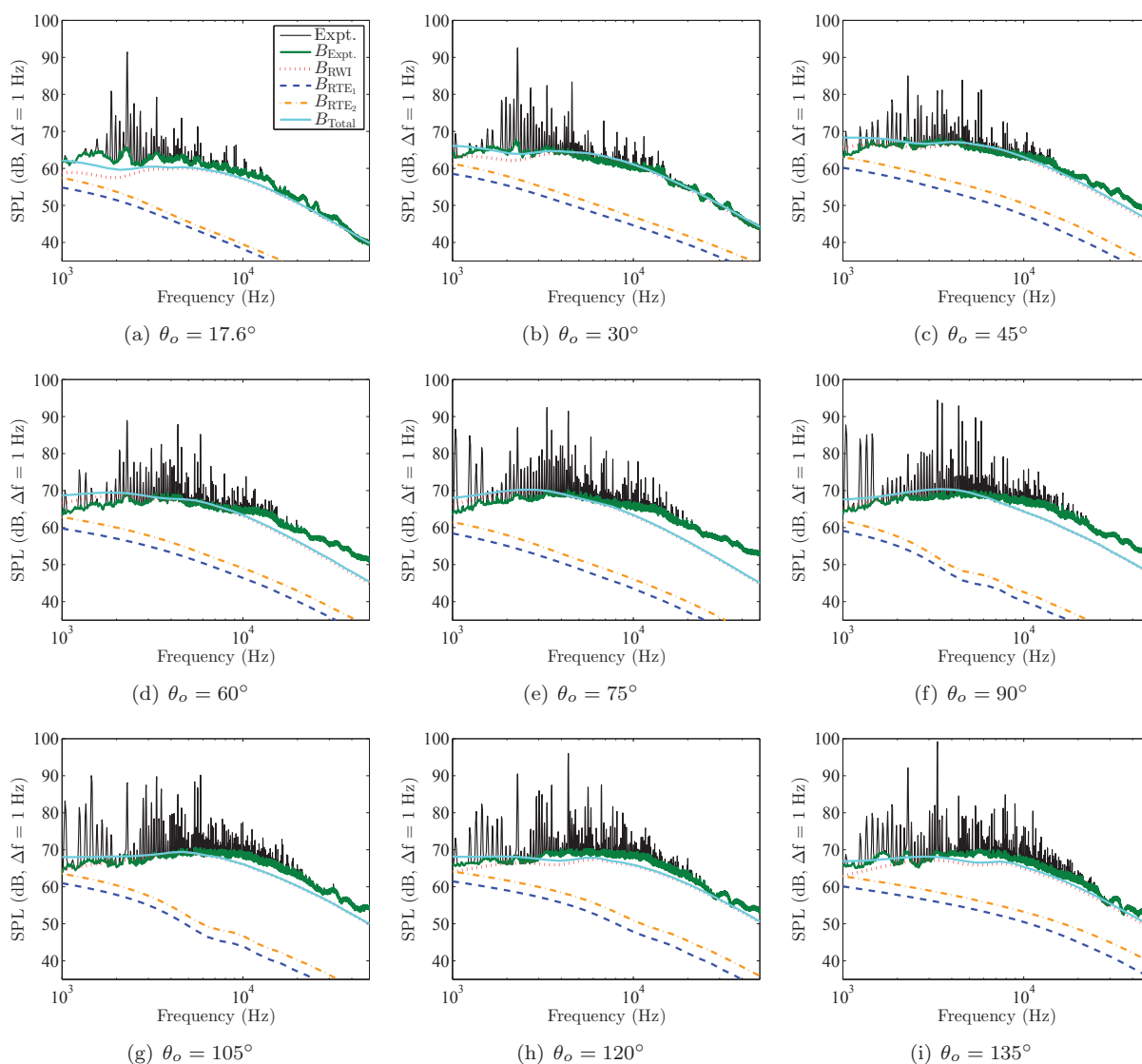

(a) $\theta_o = 17.6°$ (b) $\theta_o = 30°$ (c) $\theta_o = 45°$

(d) $\theta_o = 60°$ (e) $\theta_o = 75°$ (f) $\theta_o = 90°$

(g) $\theta_o = 105°$ (h) $\theta_o = 120°$ (i) $\theta_o = 135°$

Figure 12. CROR broadband noise predictions at select observer angles for intermediate take-off condition (Ω = 6068 RPM). Predictions are generated using the ADT-BEA in-flow model.

American Institute of Aeronautics and Astronautics

Figure 13 displays the OASPL noise component breakdown with comparison to experiment for the case of $\Omega = 6068$ RPM. This case shows a slightly better prediction than the $\Omega = 6436$ RPM case discussed in the previous section. This is possibly because the combined resultant velocities and angles of attack encountered by the blade sections are at the upper limit of the capabilities of the XFOIL software for the former case, which could lead to uncertainties in the force coefficient and boundary layer displacement thickness values predicted by XFOIL. The current result displays an excellent agreement in directivity trends with the experiment, with a maximum discrepancy of 1.7 dB at $\theta_o = 120°$.
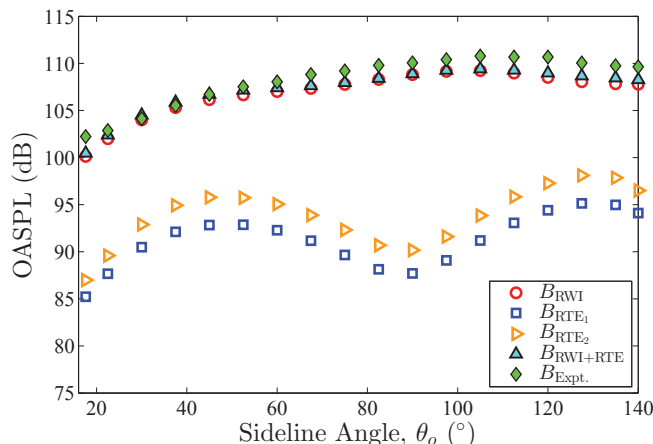
Figure 13. Broadband OASPL component breakdown for intermediate take-off condition ($\Omega = 6068$ RPM) with comparison to experiment. Predictions are generated using the ADT-BEA in-flow model.

C.   Broadband Source Contributions for Different Flight Conditions

The blade element analysis performed in this study has important limitations, namely its two-dimensional nature as well as its limited subsonic regime of application. These limitations therefore prevent the method from being applied to a cruise condition in which rotor tip speeds can become supersonic. It is arguable, however, that such a flight condition will be dominated by tonal noise and diminish the concern for the broadband contributions. The flight conditions primarily emphasized in this study are representative of the take-off phase of an aircraft due to favorable signal-to-noise ratios (SNRs) of the broadband levels measured in the experiments. Poor SNRs of broadband levels measured for approach conditions make comparisons between prediction and experiment unreliable. However, the prediction method should still be applicable to an approach condition. Therefore, predictions are made to determine the contributions of the different broadband source mechanisms to the overall broadband noise levels for these different flight conditions.

Figure 14 presents the spectral prediction results for a nominal take-off and approach condition using the simple ADT-BEA in-flow model. As Figs. 14(a) and 14(c) show, the BRWI component of noise is the dominant source mechanism for take-off across the majority of the computed frequency range. Observation of Figs. 14(b) and 14(d) show, however, that the BRTE noise of the front and aft rotor blades becomes a more important noise source at low and high frequencies for the approach configuration. The noise due to BRTE is seen to be lowest near $\theta_o = 90°$ (in the plane of the rotor) for both conditions, exhibiting a more traditional dipole directivity behavior. BRWI, meanwhile is seen to be less directive in nature, showing much less variation in amplitude with observation angle. This change in balance of the broadband source mechanisms between flight conditions can be related to the loading experienced by the front rotor. The combination of higher velocities and angles of attack at take-off as compared to approach result in considerably wider turbulent wakes that yield higher peak levels of BRWI at lower frequencies. During approach, the front rotor blades generate narrower wakes indicative of lower drag coefficients, greatly reducing the lower frequency BRWI noise. As for BRTE noise, the reduction in total velocity and angles of attack experienced by both blade rows during approach produces smaller suction side trailing edge displacement thicknesses, while also slightly increasing those on the pressure side. This results in an overall decrease in spectral BRTE levels that is less sensitive to the loading conditions of the front rotor.
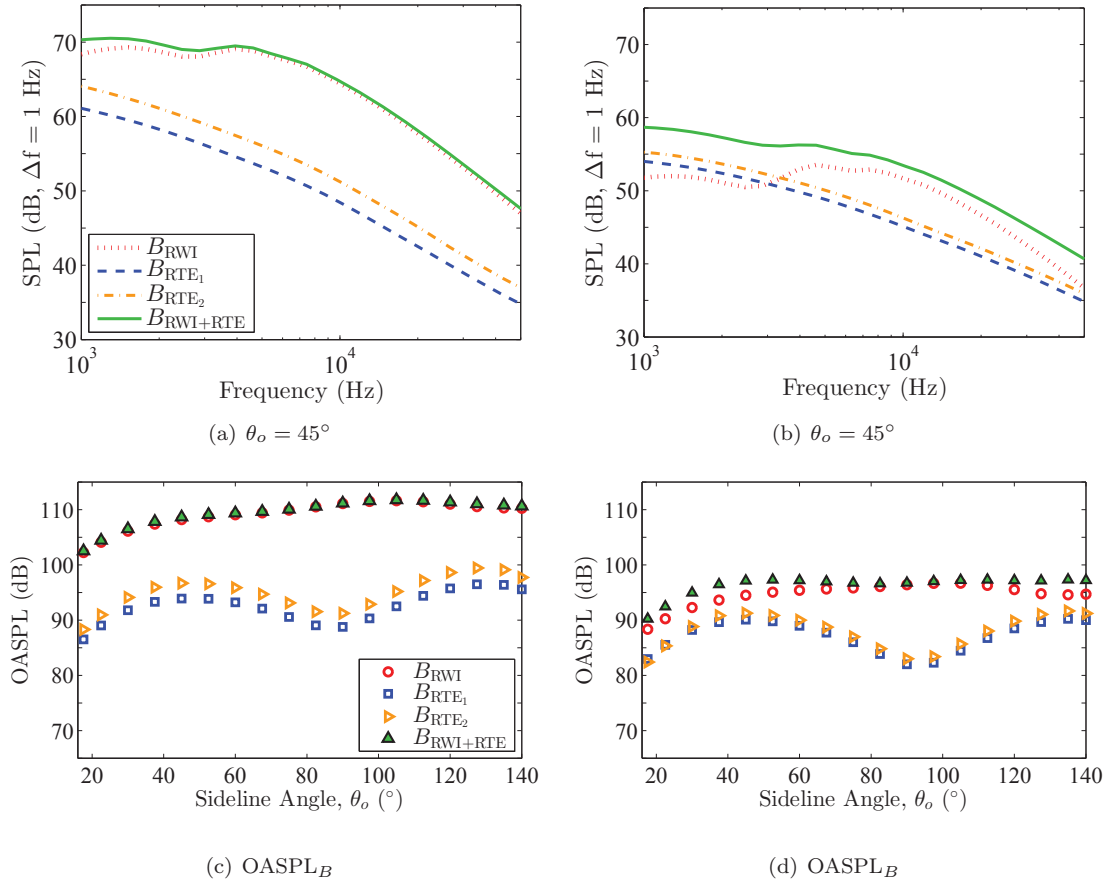
Figure 14. CROR broadband noise predictions for (a), (c) nominal take-off condition (Ω = 6436 RPM) and (b), (d) nominal approach condition (Ω = 5589 RPM). Top row displays spectral predictions at $\theta_o = 45°$, bottom row displays broadband OASPLs as a function of sideline observer angle. Note: OASPLs computed over previously mentioned frequency range of $1.8 \leq f \leq 50$ kHz.

VI.   Conclusions and Future Work

The primary goal of this study is to demonstrate the ability of semi-analytical formulations to predict the broadband levels generated by CRORs. It is desired that the predictions be computed without requiring detailed flow data from CFD. This is desired so that these computationally efficient methods may be applied in CROR design/optimization studies in which such CFD information is not available. Semi-analytical formulations for CROR BRWI and BRTE noise generation were computed and compared to experimental acoustic measurements of the F31/A31 historical baseline configuration. A blade element analysis was performed using XFOIL software with in-flow conditions provided by either CFD data or traditional combined rotorcraft momentum and blade element theories to compute the aerodynamic inputs required by the broadband formulations.

Spectral results for several rotor operating conditions were examined and found to yield overall good agreement in spectral trends and amplitudes with those observed in experimental measurements. It was found that slightly better predictions are attainable with the use of CFD in-flow information from an absolute level standpoint; however, very similar broadband directivity trends are observed for all in-flow models. It is further evidenced that there is very little difference in integrated broadband levels between using an axial induced velocity variation as a function of span along the blade and a single value determined from actuator disk theory. This implies that the use of a simple ADT-BEA for the induced velocity behavior is adequate for capturing the broadband trends of a CROR configuration. The results further indicate that the broadband noise associated with a nominal take-off condition is dominated by BRWI noise, while that associated with

American Institute of Aeronautics and Astronautics

a nominal approach condition consists of comparable BRWI and BRTE contributions for certain angles of observation.

Future work could include the implementation of a blade element analysis using a software platform more suited for the transonic flow regime encountered by CROR blades at high rotational speeds, as well as for the cascade arrangement of the rotor blades. Possible software platforms for these respective purposes are MSES[32] and MISES.[33] The blade element analysis can also be improved to include blade elements of variable size to allow reliable BRTE predictions down to lower frequencies of interest. The broadband predictions could be expanded to include installation effects such as the placement of a pylon upstream of the front rotor.[34] Future work could also include additional CFD simulations of off-condition CROR flight cases to identify variability of in-flow trends as functions of both rotor speed and blade pitch. The simulations could be used for tonal acoustic predictions that could be compared to experimental measurements. The empirical CROR tonal prediction code CRPFAN[3] could also be tested and compared to experimental results. Pending favorable comparisons with experiments, CRPFAN and the current broadband prediction schemes could be expected to be combined to yield a complete noise prediction toolkit for future design work of CRORs.

References

[1]Guynn, M. D., Berton, J. J., Haller, W. J., Hendricks, E. S., and Tong, M. T., "Performance and Environmental Assessment of an Advanced Aircraft with Open Rotor Propulsion," 2012, NASA TM Report 2012-217772.

[2]Hanson, D. B., "Noise of counter-rotation propellers," *Journal of Aircraft*, Vol. 22, No. 7, July 1985, pp. 609–617.

[3]Whitfield, C. E., Mani, R., and Gliebe, P. R., "High Speed Turboprop Aeroacoustic Study (Counterrotation) Volume I - Model Development," 1990, NASA Contractor Report 185241.

[4]Parry, A. B. and Vianello, S., "A project study of open rotor noise," *International Journal of Aeroacoustics*, Vol. 11, No. 2, June 2012, pp. 247–258.

[5]Parry, A. B., Kingan, M. J., and Tester, B. J., "Relative importance of open rotor tone and broadband noise sources," *17th AIAA/CEAS Aeroacoustics Conference*, AIAA, Portland, Oregon, 2011, AIAA Paper 2011-2763.

[6]Envia, E., "Open Rotor Aeroacoustic Modelling," *15th International Conference on Fluid Flow Technologies*, Budapest, Hungary, 2012.

[7]Bahr, C. J., Thomas, R. H., Lopes, L. V., Burley, C. L., and Van Zante, D. E., "Open Rotor Tone Shielding Methods for System Noise Assessments Using Multiple Databases," *52nd Aerospace Sciences Meeting (AIAA SciTech)*, AIAA, National Harbor, MD, 2014, AIAA Paper 2014-0367.

[8]Blandeau, V. P., Joseph, P. F., Kingan, M. J., and Parry, A. B., "Broadband noise predictions from uninstalled contra-rotating open rotors," *International Journal of Aeroacoustics*, Vol. 12, No. 3, Jan. 2013, pp. 245–282.

[9]Johnson, W., "Induced Power in Vertical Flight," *Rotorcraft Aeromechanics*, edited by W. Shyy and V. Yang, chap. 4, Cambridge University Press, New York, NY, 1st ed., 2013, pp. 92–101.

[10]Blandeau, V., *Aerodynamic Broadband Noise from Contra-Rotating Open Rotors*, Dissertation, University of Southampton, 2011.

[11]Blandeau, V. P. and Joseph, P. F., "Broadband Noise Due to Rotor-Wake/Rotor Interaction in Contra-Rotating Open Rotors," *AIAA Journal*, Vol. 48, No. 11, Nov. 2010, pp. 2674–2686.

[12]Ffowcs Williams, J. and Hawkings, D., "Theory relating to the noise of rotating machinery," *Journal of Sound and Vibration*, Vol. 10, No. 1, July 1969, pp. 10–21.

[13]Drela, M., "XFOIL: An Analysis and Design System for Low Reynolds Number Airfoils," *Low Reynolds Number Aerodynamics*, edited by T. Mueller, Vol. 54 of *Lecture Notes in Engineering*, Springer Berlin Heidelberg, 1989, pp. 1–12.

[14]Amiet, R. K., "Acoustic Radiation from an Airfoil in a Turbulent Stream," *Journal of Sound and Vibration*, Vol. 41, No. 4, 1975, pp. 407–420.

[15]Moreau, S. and Roger, M., "Competing Broadband Noise Mechanisms in Low Speed Axial Fans," *10th AIAA/CEAS Aeroacoustics Conference*, AIAA, Manchester, United Kingdom, 2004, AIAA Paper 2004-3039.

[16]Amiet, R. K., "Noise Produced by Turbulent Flow Into a Rotor: Theory Manual for Noise Calculation," 1989, NASA CR Report 181788.

[17]Kim, Y. N. and George, A. R., "Trailing-Edge Noise from Hovering Rotors," *AIAA Journal*, Vol. 20, No. 9, 1982, pp. 1167–1174.

[18]Roger, M. and Moreau, S., "Back-scattering correction and further extensions of Amiet's trailing-edge noise model. Part 1: theory," *Journal of Sound and Vibration*, Vol. 286, Sept. 2005, pp. 477–506.

[19]Jurdic, V., Joseph, P., and Antoni, J., "Investigation of Rotor Wake Turbulence Through Cyclostationary Spectral Analysis," *AIAA Journal*, Vol. 47, No. 9, Sept. 2009, pp. 2022–2030.

[20]Gliebe, P., Mani, R., Shin, H., Mitchell, B., Ashford, G., Salamah, S., and Connell, S., "Aeroacoustic Prediction Codes," 2000, NASA CR 210244.

[21]Wygnanski, I., Champagne, F., and Marasli, B., "On the large-scale structures in two-dimensional, small-deficit, turbulent wakes," *Journal of Fluid Mechanics*, Vol. 168, April 1986, pp. 31–71.

[22]Rozenberg, Y., Roger, M., and Moreau, S., "Rotating Blade Trailing-Edge Noise: Experimental Validation of Analytical Model," *AIAA Journal*, Vol. 48, No. 5, May 2010, pp. 951–962.

[23]Corcos, G. M., "The structure of the turbulent pressure field in boundary-layer flows," *Journal of Fluid Mechanics*, Vol. 18, No. 3, 1964, pp. 353–378.

[24] Brooks, T. F. and Hodgson, T. H., "Trailing Edge Noise Prediction from Measured Surface Pressures," *Journal of Sound and Vibration*, Vol. 78, No. 1, 1981, pp. 69–117.

[25] Van Zante, D. E. and Wernet, M. P., "Tip Vortex and Wake Characteristics of a Counterrotating Open Rotor," *18th AIAA/CEAS Aeroacoustics Conference*, AIAA, Colorado Springs, CO, 2012, AIAA Paper 2012-4039.

[26] Johnson, W., "Blade Element Theory," *Rotorcraft Aeromechanics*, edited by W. Shyy and V. Yang, chap. 3, Cambridge University Press, New York, NY, 1st ed., 2013, pp. 52–60.

[27] Johnson, W., *Hover: Extended Momentum Theory*, chap. 3, Cambridge University Press, 2013, pp. 45–52.

[28] Whitfield, C. E., Gliebe, P. R., Mani, R., and Mungur, P., "High Speed Turboprop Aeroacoustic Study (Single Rotation)," 1989, NASA CR 182257.

[29] Buning, P. G., "CFD Approaches for Simulation of Wing-Body Stage Separation," *22nd Applied Aerodynamics Conference and Exhibit*, No. August, AIAA, Providence, RI, 2004, AIAA Paper 2004-4838.

[30] Boyd, D. D., "HART-II Acoustic Predictions using a Coupled CFD / CSD Method," *American Helicopter Society 65th Annual Forum*, Grapevine, TX, 2009.

[31] Glegg, S. A. L., Devenport, W., Wittmer, K. S., and Pope, D. S., "Broadband Helicopter Noise Generated by Blade Wake Interactions," *Proceedings of the American Helicopter Society Technical Specialists' Meeting For Rotorcraft Acoustics and Aerodynamics*, Williamsburg, VA, 1997.

[32] Smith, M. J., Wong, T.-c., Potsdam, M. A., Baeder, J., and Phanse, S., "Evaluation of CFD to Determine Two-Dimensional Airfoil Characteristics for Rotorcraft Applications," *Journal of the American Helicopter Society*, Vol. 51, No. 1, 2006, pp. 70–79.

[33] Drela, M. and Youngren, H., "A Users Guide to MISES 2.63," 2008.

[34] Kingan, M. J., "Open Rotor Broadband Interaction Noise," *18th AIAA/CEAS Aeroacoustics Conference*, AIAA, Colorado Springs, CO, 2012, AIAA Paper 2012-2304.